

## **Development of the self-referencing interferometer wavefront sensor (Postprint)**

**Troy A. Rhoadarmer**

**30 July 2004**

### **Conference Proceedings**

**APPROVED FOR PUBLIC RELEASE; DISTRIBUTION IS UNLIMITED.**



**AIR FORCE RESEARCH LABORATORY  
Directed Energy Directorate  
3550 Aberdeen Ave SE  
AIR FORCE MATERIEL COMMAND  
KIRTLAND AIR FORCE BASE, NM 87117-5776**

---

# REPORT DOCUMENTATION PAGE

Form Approved  
OMB No. 0704-0188

Public reporting burden for this collection of information is estimated to average 1 hour per response, including the time for reviewing instructions, searching existing data sources, gathering and maintaining the data needed, and completing and reviewing this collection of information. Send comments regarding this burden estimate or any other aspect of this collection of information, including suggestions for reducing this burden to Department of Defense, Washington Headquarters Services, Directorate for Information Operations and Reports (0704-0188), 1215 Jefferson Davis Highway, Suite 1204, Arlington, VA 22202-4302. Respondents should be aware that notwithstanding any other provision of law, no person shall be subject to any penalty for failing to comply with a collection of information if it does not display a currently valid OMB control number. PLEASE DO NOT RETURN YOUR FORM TO THE ABOVE ADDRESS.

<b>1. REPORT DATE</b> (DD-MM-YYYY) 30-07-2004		<b>2. REPORT TYPE</b> Conference Proceedings		<b>3. DATES COVERED</b> (From - To) 1 Apr 02 - 1 Jul 04	
<b>4. TITLE AND SUBTITLE</b> Development of the self-referencing interferometer Wavefront sensor (Postprint)				<b>5a. CONTRACT NUMBER</b> In House- 299962	<b>5b. GRANT NUMBER</b>
				<b>5c. PROGRAM ELEMENT NUMBER</b> 063605F	<b>5d. PROJECT NUMBER</b> JT00
<b>6. AUTHOR(S)</b> Troy A. Rhoadarmer				<b>5e. TASK NUMBER</b> S0	<b>5f. WORK UNIT NUMBER</b> AB
<b>7. PERFORMING ORGANIZATION NAME(S) AND ADDRESS(ES)</b>  AFRL/DES 3550 Aberdeen Ave SE Kirtland AFB, NM 87117-5776				<b>8. PERFORMING ORGANIZATION REPORT NUMBER</b>	
<b>9. SPONSORING / MONITORING AGENCY NAME(S) AND ADDRESS(ES)</b> AIR FORCE RESEARCH LABORATORY 3550 Aberdeen Ave SE Kirtland AFB, NM 87117-5776				<b>10. SPONSOR/MONITOR'S ACRONYM(S)</b> AFRL/DES	
				<b>11. SPONSOR/MONITOR'S REPORT NUMBER(S)</b> AFRL-DE-PS-TP-2007-1010	
<b>12. DISTRIBUTION / AVAILABILITY STATEMENT</b>  Approved for Public Release; Distribution is Unlimited.					
<b>13. SUPPLEMENTARY NOTES</b> Published in Proceedings of SPIE, Advanced Wavefront Control: methods, Devices, and Application II, Vol. 5553, pp. 112-126, 12 October 2004. GOVERNMENT PURPOSE RIGHTS					
<b>14. ABSTRACT</b> The self-referencing Interferometer (SRI) is an innovative wavefront sensor (WFS) developed specifically for applications requiring laser propagation in strong scintillation. The performance of conventional gradient sensors, like a Shack-Hartmann WFS or lateral shearing interferometer, are severely limited in these environments due to the presence of branch points in the wavefront phase. Unlike these sensors, the SRI WFS directly measures the wavefront field so that its performance is not affected by the presence of branch points. Over the last two years under funding from the High Energy Laser Joint Technology Office, the Starfire Optical Range has been developing a prototype SRI WFS to demonstrate its advantages in strong scintillation environments. This paper discusses practical lessons learned in building an operating an SRI WFS and presents initial results from laboratory tests.					
<b>15. SUBJECT TERMS</b> Adaptive optics, wavefront sensors, interferometer, scintillation					
<b>16. SECURITY CLASSIFICATION OF:</b>			<b>17. LIMITATION OF ABSTRACT</b> SAR	<b>18. NUMBER OF PAGES</b> 17	<b>19a. NAME OF RESPONSIBLE PERSON</b> Troy Rhoadarmer
<b>a. REPORT</b> Unclassified	<b>b. ABSTRACT</b> Unclassified	<b>c. THIS PAGE</b> Unclassified			<b>19b. TELEPHONE NUMBER</b> (include area code)

# Development of a self-referencing interferometer wavefront sensor

Troy A. Rhoadarmer

Beam Control Division, AFRL/DES, Directed Energy Directorate,  
U.S. Air Force Research Laboratory, Kirtland AFB, NM 87117-5776 USA

## ABSTRACT

The self-referencing interferometer (SRI) is an innovative wavefront sensor (WFS) developed specifically for applications requiring laser propagation in strong scintillation. The performance of conventional gradient sensors, like Shack-Hartmann WFSs or lateral shearing interferometers, are severely limited in these environments due to the presence of branch points in the wavefront phase. In comparison, the SRI WFS directly measures the wavefront field so its performance is not affected by the presence of branch points. Over the last two years the Starfire Optical Range has been developing a prototype SRI WFS to demonstrate its advantages in strong scintillation environments. This paper discusses some practical lessons learned in building and operating an SRI WFS and presents initial results from laboratory tests.

**Keywords:** adaptive optics, wavefront sensors, interferometers, scintillation

## 1. INTRODUCTION

The wavefront sensor (WFS) is an important component of any adaptive-optical (AO) system. Its performance directly affects the achievable Strehl ratio of the entire system. Many current AO systems rely on either a Shack-Hartmann WFS or a lateral shearing interferometer coupled with a least-squares reconstructor to estimate wavefront aberrations.<sup>1</sup> Unfortunately, the performance of these systems degrades severely in strong scintillation due to the presence of branch points in the wavefront phase.<sup>2-5</sup> This reduction in estimation accuracy makes these WFS systems of limited use in applications which operate in extended turbulence conditions.

In this paper we describe an innovative WFS concept that offers a solution to the wavefront sensing problem in strong scintillation—the self-referencing interferometer (SRI) WFS with an amplified reference. Over the last two years, the Starfire Optical Range (SOR), Directed Energy Directorate, Air Force Research Laboratory, has been developing a prototype SRI WFS under funding from the High Energy Laser Joint Technology Office. In the first phase of the project we performed an in-depth analysis of the predicted performance of the SRI WFS.<sup>6,7</sup> As summarized below in section 2, its performance is theoretically immune to scintillation. In the second phase we have been constructing a laboratory test facility to demonstrate the SRI WFS and evaluate its performance. Some of the practical lessons learned in building and operating a SRI WFS are discussed in section 3. The laboratory system is described in section 4 and some initial test results are presented in section 5.

## 2. OVERVIEW OF THE SRI WFS

The SRI WFS is based on a phase-shifting, point diffraction interferometer.<sup>8</sup> Figure 1 shows a conceptual diagram of the SRI WFS. The incoming optical field is split into two beams, the beacon and the reference. The reference is coupled into a single mode fiber that spatially filters the beam and produces a known field at the fiber output. After traveling equidistant paths, the beacon and filtered reference beams are recombined at the WFS camera where they produce interferometric fringes. To boost the amplitude of the fringes, an optical amplifier is placed in the reference fiber path. An inline phase shifter is also used in the fiber path to control the phase of the reference.

In the absence of noise and assuming perfect coherence, the intensity measured for the  $n$ -th phase shift in the  $m$ -th subaperture of the SRI WFS is given by

$$I_n(x_m, y_m) = \iint_{A_m} dx dy |U_b(x, y) + U_r(x, y)e^{-i\theta_n}|^2, \quad (1)$$

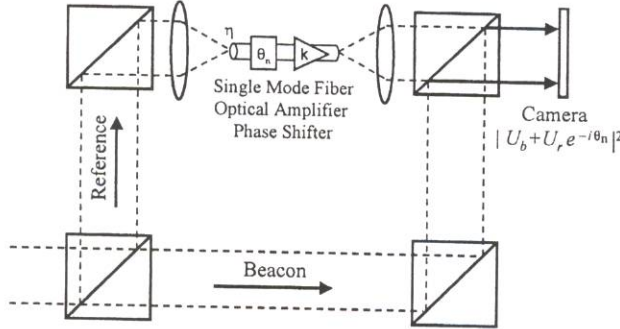


Figure 1. Conceptual diagram of the SRI WFS.

where  $(x_m, y_m)$  is the subaperture center position and integration is over the subaperture area  $\mathcal{A}_m$ .  $U_b(x, y)$  is the beacon field.  $U_r(x, y)$  is the reference field including the effects of fiber coupling efficiency  $\eta$  and optical amplification  $k$ , and  $e^{-i\theta_n}$  represents the phase shift applied to the reference. Defining the beacon and reference fields as

$$U_b(x, y) = A_b(x, y)e^{i\phi_b(x, y)} \quad (2)$$

$$U_r(x, y) = A_r(x, y), \quad (3)$$

where it is assumed the reference has zero phase, equation 1 becomes

$$I_n(x_m, y_m) = \iint_{\mathcal{A}_m} dx dy [A_b^2(x, y) + A_r^2(x, y) + 2A_b(x, y)A_r(x, y)\cos(\phi_b + \theta_n)]. \quad (4)$$

Using  $\theta_n = [0, \pi/2, \pi, 3\pi/2]$  for the set of phase shifts, the beacon field is estimated from the intensities as<sup>8</sup>

$$\hat{U}_b(x_m, y_m) = \frac{1}{4\mathcal{A}_m} \{ [I_1(x_m, y_m) - I_3(x_m, y_m)] + i[I_4(x_m, y_m) - I_2(x_m, y_m)] \} \quad (5)$$

$$= \frac{1}{\mathcal{A}_m} \iint_{\mathcal{A}_m} dx dy A_r(x, y)A_b(x, y)e^{i\phi_b(x, y)}, \quad (6)$$

where ‘~’ indicates an estimate. Further assuming a uniform reference with unity amplitude (i.e.,  $A_r(x, y) = 1$ ) and using equation 2, the field estimate becomes

$$\hat{U}_b(x_m, y_m) = \frac{1}{\mathcal{A}_m} \iint_{\mathcal{A}_m} dx dy U_b(x, y), \quad (7)$$

indicating the SRI WFS measures the average field over each subaperture. Furthermore, estimates of the amplitude and phase of the beacon field can be found from

$$\hat{A}_b(x_m, y_m) = |\hat{U}_b(x_m, y_m)| = \frac{1}{4\mathcal{A}_m} \sqrt{[I_1(x_m, y_m) - I_3(x_m, y_m)]^2 + [I_4(x_m, y_m) - I_2(x_m, y_m)]^2} \quad (8)$$

$$\hat{\phi}_b(x_m, y_m) = \arg \{ \hat{U}_b(x_m, y_m) \} = \arctan \left( \frac{I_4(x_m, y_m) - I_2(x_m, y_m)}{I_1(x_m, y_m) - I_3(x_m, y_m)} \right), \quad (9)$$

where the result of the arctangent is between  $-\pi$  and  $\pi$ . By aligning the actuators of a deformable mirror (DM) with the subaperture centers as shown in figure 2(a), the estimated phase can be used to close an AO control loop. (Diagram (b) of figure 2, showing a high-resolution SRI WFS, is discussed in section 3.5.)

As shown in equation 7, the SRI WFS measures the average complex field of the beacon wavefront directly. This feature is very advantageous in the presence of scintillation. The performance of the SRI WFS can be evaluated at the subaperture centers with a field estimation Strehl defined by

$$S_{est} = \frac{|\langle U_b(x_m, y_m) \hat{U}_b^*(x_m, y_m) \rangle_m|^2}{\langle |U_b(x_m, y_m)|^2 \rangle_m \langle |\hat{U}_b(x_m, y_m)|^2 \rangle_m}, \quad (10)$$

where ‘ $\langle \cdot \rangle_m$ ’ is the expectation operator averaged over all values of  $m$  and ‘\*’ indicates the complex conjugate.<sup>7</sup>

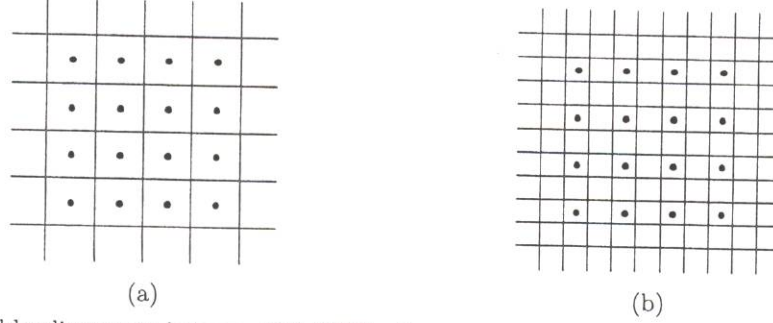


**Figure 2.** Possible alignments between SRI WFS subapertures and DM actuators. The squares indicate WFS subaperture boundaries and the dots show the positions of the DM actuators. The diagrams illustrate (a) a one-to-one alignment scheme and (b) a high-resolution arrangement which helps improve control loop stability in strong turbulence.

This Strehl is equivalent to the Strehl ratio that would be obtained by a full-wave compensation system that perfectly compensates the field  $\hat{U}_b$ . Evaluation of this expression begins by defining the autocorrelation function

$$\mathcal{U}(x, y) = \langle U_b(u - x, v - y) U_b^*(u, v) \rangle_{uv}, \quad (11)$$

where the expectation is calculated over  $(u, v)$ . Using this function, the first term in the denominator is

$$\langle |U_b(x_m, y_m)|^2 \rangle_m = \mathcal{U}(0, 0). \quad (12)$$

By applying equation 7, the second term in the denominator becomes

$$\langle |\hat{U}_b(x_m, y_m)|^2 \rangle_m = \frac{1}{d^4} \int_{-d/2}^{d/2} dx \int_{-d/2}^{d/2} dy \int_{-d/2}^{d/2} du \int_{-d/2}^{d/2} dv \langle U_b(x - x_m, y - y_m) U_b^*(u - x_m, v - y_m) \rangle_m \quad (13)$$

$$= \frac{1}{d^4} \int_{-d/2}^{d/2} dx \int_{-d/2}^{d/2} dy \int_{-d/2}^{d/2} du \int_{-d/2}^{d/2} dv \mathcal{U}(u - x, v - y), \quad (14)$$

where square subapertures of size  $d$  (i.e.,  $\mathcal{A}_m = d^2$ ) are assumed and the positions  $(x, y)$  and  $(u, v)$  are measured relative to the subaperture center. As described in reference [7], by exploiting the symmetries of the autocorrelation and performing a change of variables, equation 14 can be simplified into the expression

$$\langle |\hat{U}_b(x_m, y_m)|^2 \rangle_m = 4 \int_0^1 d\alpha \int_0^1 d\beta \mathcal{U}(d\alpha, d\beta) (1 - \alpha) (1 - \beta). \quad (15)$$

Using similar techniques, the expectation in the numerator is evaluated as

$$\langle U_b(x_m, y_m) \hat{U}_b^*(x_m, y_m) \rangle_m = \frac{1}{d^4} \int_{-d/2}^{d/2} dx \int_{-d/2}^{d/2} dy \langle U_b(x_m, y_m) \hat{U}_b^*(x - x_m, y - x_m) \rangle_m \quad (16)$$

$$= \frac{1}{d^4} \int_{-d/2}^{d/2} dx \int_{-d/2}^{d/2} dy \mathcal{U}(x, y) \quad (17)$$

$$= 4 \int_0^{1/2} d\alpha \int_0^{1/2} d\beta \mathcal{U}(d\alpha, d\beta), \quad (18)$$

For Kolmogorov turbulence,  $\mathcal{U}(x, y) = \exp \left[ -3.44 \left( \sqrt{x^2 + y^2} / r_0 \right)^{5/3} \right]$ , where  $r_0$  is the atmospheric coherence length, and the estimation Strehl is<sup>9</sup>

$$S_{est} = \frac{4 \left| \int_0^{1/2} d\alpha \int_0^{1/2} d\beta \exp \left[ -3.44 \left( \frac{d\sqrt{\alpha^2 + \beta^2}}{r_0} \right)^{5/3} \right] \right|^2}{\int_0^1 d\alpha \int_0^1 d\beta (1 - \alpha) (1 - \beta) \exp \left[ -3.44 \left( \frac{d\sqrt{\alpha^2 + \beta^2}}{r_0} \right)^{5/3} \right]}. \quad (19)$$

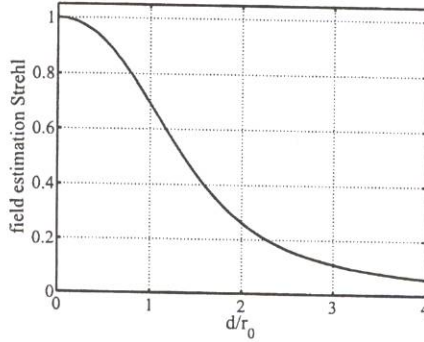


**Figure 3.** Field estimation Strehl for the SRI WFS with Kolmogorov turbulence.

This expression can be evaluated numerically as shown in figure 3. The analysis shows that the ability of the SRI WFS to estimate the beacon field depends only on the ratio of the subaperture size to the atmospheric coherence length. Unlike a Shack-Hartmann WFS or a lateral shearing interferometer, SRI WFS performance does not depend on the strength of scintillation. It should be noted that this plot corresponds to open-loop wavefront sensing performance. In stable closed-loop operation, the effective  $r_0$  of the residual wavefront is larger,  $d/r_0$  is smaller, and WFS performance should improve.

### 3. PRACTICAL ISSUES

The above analysis shows SRI WFS performance is immune to scintillation. However, the analysis is idealized in that it does not consider practical concerns such as noise and coherence. This section discusses some of those issues and how they impact the fabrication and operation of the SRI WFS. While there are many issues, the ones presented are of particular relevance to the SRI WFS, as compared to WFSs and AO systems in general.

#### 3.1. Optical amplification

The SRI WFS utilizes an optical amplifier to boost the amplitude of the reference beam and increase the depth of the interference fringes on the WFS camera. A noise analysis has shown that amplification is needed to overcome read noise and quantization noise on the WFS camera so as to produce and maintain a sufficient signal-to-noise ratio for stable closed-loop operation.<sup>6</sup> For lower-noise cameras, less gain is required. The amplifier assists in initially closing the AO control loop and helps maintain stable loop operation when the coupling efficiency of the reference beam into the fiber degrades temporarily. During open-loop operation, the fiber coupling efficiency can be very small for severely aberrated input beams. In strong turbulence, tracking alone may not be sufficient to produce a reference beam strong enough to create fringes that can be detected above the camera noise. Computer simulations have shown that without amplification the AO loop may not close or may take a very long time to close. However, with amplification the AO loop can more easily begin to close. Once that occurs, wavefront correction improves and more light is coupled into the fiber. The increased coupling efficiency produces a corresponding increase in SRI WFS performance. Tracking performance will also improve due to a smaller spot on the track sensor. This snowball-like effect continues until the AO loop reaches stable, closed-loop operation.

While amplification makes the SRI WFS work better, it also comes with its own unique set of problems. One of the primary issues affecting SRI WFS performance is amplified spontaneous emission (ASE), which occurs as a result of pumping the amplifier gain medium. The ASE power is given by

$$P_{ASE} = (k - 1) NF \left( \frac{\Delta\lambda c}{\lambda^2} \right) \left( \frac{hc}{\lambda} \right), \quad (20)$$

where  $k$  is the gain,  $NF$  is the noise figure,  $\lambda$  is the nominal ASE wavelength,  $\Delta\lambda$  is the width of the ASE wavelength spectrum,  $c$  is the speed of light, and  $h$  is Planck's constant. The gain and noise figure are generally reported in dB but are used in their multiplicative form in this equation. Fortunately, ASE is incoherent with respect to the beacon and reference beams and does not affect the shape of the interference fringes. However, it

does introduce background light that reduces fringe visibility, reduces available camera well depth and resolution, and contributes shot noise to the intensity measurements. Because of these effects, ASE limits the minimum detectable beacon power and creates the possibility of having too much amplification resulting in less than optimal WFS performance.<sup>6</sup> Determining the appropriate level of amplification is important when designing a SRI WFS. ASE can be reduced by decreasing the gain  $k$ , noise figure  $NF$ , or spectral bandwidth  $\Delta\lambda$ . While  $k$  and  $NF$  are properties of the amplifier, a narrow-band spectral filter can provide an independent means of reducing ASE. Also, if the beacon and reference beams are polarized, ASE can be further reduced by using polarizers.

There are a couple of types of optical amplifiers from which to choose. The SRI WFS laboratory demonstration under development at the SOR operates at a wavelength of  $\lambda = 1.55\mu m$ . Erbium-doped fiber amplifiers (EDFAs) and semiconductor optical amplifiers (SOAs) are readily available for the C-band ( $1.53\mu m < \lambda < 1.57\mu m$ ). There are some basic tradeoffs between these two amplifiers. Commercially, EDFAs have higher available gains (30-50 dB) compared to SOAs (15-25 dB). In addition, EDFAs have lower noise figures (3-5 dB) compared to SOAs (9-12 dB). This comparison seems to indicate that an EDFA would be the preferred choice, especially since a smaller  $NF$  means the SRI WFS can operate at lower illumination levels.<sup>6</sup> However, EDFAs also have much longer optical path lengths ( $> 10$  m) compared to SOAs ( $< 2$  cm) and they are generally more expensive. The choice of which amplifier is best depends on the specific application under consideration.

An amplifier that combines the high-gain, low-noise features of an EDFA with the short optical path of a SOA would make the choice easier. There are a few companies developing amplifiers with this goal in mind. In the last year, the SOR has teamed with NP Photonics of Tucson, Arizona, to advance their mini-EDFA technology for application to the SRI WFS. A prototype amplifier with gain of 30 dB, noise figure of 5 dB, and an optical path of about 1 m has been developed and is currently undergoing testing.

### 3.2. Phase shifting techniques

To reconstruct the beacon wavefront, phase shifts of 0,  $\pi/2$ ,  $\pi$ , and  $3\pi/2$  are applied to the reference beam. These phase shifts can be accomplished in several ways. Spatial phase shifting allows all four measurements to be captured simultaneously. With this option, the reference and beacon beams are each divided into four beams with the proper phase shifts applied using static optics. The resulting interference patterns are created either on four separate detectors or on four regions of the same detector. Alternatively, the four phase shifts can be applied temporally using a fiber phase shifter as mentioned in section 2. For each phase shift, an interference pattern is measured on a single detector array and the required images are captured sequentially in four integration cycles. A combination of spatial and temporal phase shifting is also possible. In this configuration, the two interference patterns created by the last beam splitter shown in figure 1 are imaged onto separate detector arrays. These two patterns will differ by a  $\pi$  phase shift. Phase shifts of 0 and  $\pi/2$  are applied with the fiber phase shifter on alternating frames to create the four required interference images.

When deciding which phase shifting method to implement, several tradeoffs should be considered. For spatial phase shifting, the beacon and reference beams are split into several beams and recombined on different detector arrays. This approach ensures the same beacon wavefront is used for all interference measurements, but it also presents some problems. First, more camera real estate and readout electronics may be needed, increasing overall system size and cost. Second, co-aligning the beams on the detectors and maintaining the proper relative phase shifts between the different images is non-trivial and makes the hardware requirements more complex. Holographic or diffractive optical elements can be used to accomplish the proper alignment and phase relationships but these tend to throw away a large portion of the available light. Third, the different detector arrays must be accurately calibrated so the gain and bias variations can be corrected before the measurements are combined to estimate the wavefront. This is particularly critical if ASE is large compared to the fringe depth. Last, non-common path aberrations in the different beams corrupt the wavefront estimation process.

In comparison, temporal phase shifting has drastically simplified requirements for optical alignment and camera calibration since, for each WFS subaperture, the same detector element is used for all four intensity measurements. The relationships between measurements are not corrupted by co-alignment issues or non-common path aberrations. Also, the same gain and bias are present in all four measurements so camera calibration is not as much of a concern if phase estimation is the primary goal of the reconstruction process (see equation 9). Furthermore, temporal phase shifting requires smaller detector arrays or, for a given amount of camera real

estate, can provide higher spatial resolution. With a given  $N \times N$  array, temporal phase shifting can operate with  $N \times N$  subapertures while spatial phase shifting would provide at most a  $\frac{N}{2} \times \frac{N}{2}$  grid of subapertures. On the other hand, for equal resolutions, temporal phase shifting provides more photons for each interference measurement. The resulting increase in signal-to-noise can positively impact performance.

Although temporal phase shifting offers several advantages over spatial phase shifting, the major concern is that atmospheric turbulence is dynamic. The field within each subaperture changes with time and will not be constant for all of the interference measurements. The result is an effective reduction in measurement bandwidth by a factor of 4 relative to the sample rate. To limit the drop in Strehl performance to 0.9 or higher, the SRI WFS sample rate must be at least 100 times the Tyler tracking frequency for an aperture the size of a WFS subaperture.<sup>6</sup> Tyler frequencies typically are not very large, but for propagations through long or strong turbulent paths with high winds, this may require sampling faster than 10 kHz. In addition, with temporal phase shifting, half of the light is lost at the beam combiner as shown in figure 1. However, it is possible to conserve this light by combining the spatial and temporal phase-shifting approaches as mentioned above. This approach provides a middle ground between the other two methods. It attempts to balance hardware complexity against performance loss due to the dynamic nature of turbulence and an efficient use of the available light.

In the end, choosing which phase shifting approach to use must be based on the benefits and risks to the particular application being developed. To help with this decision, in-depth analyses of the differing phase shift approaches and how they affect performance have been performed and are reported in references 6 and 7. In our laboratory demonstration, we plan to evaluate and compare the various phase shifting schemes.

### 3.3. Path matching

As an interferometric sensor, the SRI WFS requires coherent illumination. The incident light being measured must be temporally and spatially coherent, or at least partially so, in order to produce fringes on the WFS camera. This requirement limits the field of applications for the SRI WFS and potentially creates difficulties for those applications in which it can work. When the incident beam is split between the beacon and reference paths, the lengths of those paths must be matched to the extent that coherence between the beacon and reference beams is maintained at the SRI WFS camera. This concern may not be an issue when a cooperative beacon is available and an appropriately long-coherence source can be built into the system. A high energy laser relay mirror is an application of this type. If a cooperative source is not available, coherence and path matching once again become important concerns. The airborne laser, which uses laser light reflected from a target as the WFS beacon, falls in this category. However, even with a cooperative source, the path matching requirement may become very restrictive. For optical communications, if the communication beam is used for wavefront sensing, the beacon and reference paths must be matched to within a fraction of the length of a data bit. After splitting between the two paths, each component of the bit must arrive at the WFS camera at the same time or else the encoding of data on the beam will effectively wash out the fringes over a camera integration period.

Furthermore, path matching is an issue for the SRI WFS because it is desirable to have a small, stable, and rugged WFS which can operate in less than optimal field conditions. It is possible to match optical paths to within a few wavelengths, but this is usually accomplished in a well-controlled laboratory environment, not on an aircraft, humvee, or naval vessel. If a commercial EDFA is used for the amplifier, the physical length of the reference fiber path would be more than 10 m. Due to the refractive index of the fiber, an equivalent air path for the beacon would need to be more than 15 m long. It is not necessarily easy to squeeze that much air path into a small package. Nor would it be easy to maintain optical alignment and stability out in the field. The situation is much better if a SOA is used. The reference fiber path could be reduced to about a meter by minimizing the fiber splices between the amplifier, phase shifter, spectral filter, and any other components (e.g., polarization controllers, isolators, and fiber beamsplitters). This length is much more reasonable. However, SOAs have poorer characteristics in terms of gain and noise compared to EDFAs. It would be preferable to have the gain and noise figure of an EDFA and the size of a SOA in the same device. Therefore, we are looking into other amplifier options, like the mini-EDFA from NP Photonics.

### 3.4. Phase unwrapping

As described above, the SRI WFS directly measures the optical field of the beacon wavefront. From these data the wavefront phase can be estimated and used to control a DM in an AO system. Unfortunately, the output

of equation 9 is limited to the range  $-\pi < \hat{\phi}_b \leq \pi$ . This is not a problem if a segmented DM is used but most current AO systems rely on continuous surface DMs since they have a more highly developed technology base and infrastructure. Before it can be sent to a continuous-surface DM, the SRI WFS phase must be unwrapped.

There are many approaches to phase unwrapping. For simplicity, and to more closely match conventional AO hardware that performs phase reconstruction using a matrix-vector multiply, we have opted to use a least-squares unwrapping algorithm. The algorithm assumes that the wavefront phase has two components. That is,

$$\phi_b(x, y) = \arg \left\{ e^{i(\phi_b^{LS}(x, y) + \phi_b^{BP}(x, y))} \right\} \quad (21)$$

where  $\phi_b^{LS}$  is the unwrapped, least-squares phase and  $\phi_b^{BP}$  is the branch-point phase. As in equation 9,  $\arg\{\cdot\}$  returns a value between  $-\pi$  and  $\pi$ . These phase measurements are converted to phase differences using

$$\Delta\phi_b^x(x, y) = \arg \left\{ e^{i(\phi_b(x, y) - \phi_b(x-d, y))} \right\} \quad (22)$$

$$\Delta\phi_b^y(x, y) = \arg \left\{ e^{i(\phi_b(x, y) - \phi_b(x, y-d))} \right\}, \quad (23)$$

where  $d$  is the WFS subaperture size. These differences are ordered into a vector  $\vec{\Delta}$  which is then multiplied by a least-squares reconstruction matrix  $E$  to determine the least-squares phase vector<sup>10</sup>

$$\vec{\phi}_b^{LS} = E \vec{\Delta}, \quad (24)$$

which is then reshaped into  $\phi_b^{LS}(x, y)$ . The SRI WFS can also be used to detect branch points. The branch-point phase can be calculated with the expression

$$\phi_b^{BP}(x, y) = \arg \left\{ e^{i(\phi_b(x, y) - \phi_b^{LS}(x, y))} \right\} \quad (25)$$

Finally, the total unwrapped phase becomes

$$\phi_b^{Tot}(x, y) = \phi_b^{LS}(x, y) + \phi_b^{BP}(x, y). \quad (26)$$

The least-squares phase or the total unwrapped phase can be used to drive a DM.

This algorithm has some beneficial features. Unlike iterative approaches, it requires a finite and defined number of calculations. More importantly, it can be easily parallelized using processing architectures similar to those used on several current AO systems. We are looking at other, potentially better, phase unwrapping algorithms, but for now the least-squares solution is sufficient.

### 3.5. Wavefront sensing resolution

The last practical issue to be addressed in this section deals with the sampling resolution of the SRI WFS. The SRI WFS measures the average field within each subaperture but, while this feature makes its performance immune to scintillation, it has a negative aspect to it. When large enough, tilt becomes a poorly sensed mode similar to the waffle mode for a Shack-Hartmann WFS. The problem is illustrated by considering how the SRI WFS responds to a uniform plane wave having one wave (2π radians) of tilt across a subaperture. In this case the average field in the subaperture is zero and the WFS output may artificially indicate the presence of a branch point in the subaperture that can corrupt the phase reconstruction process.

There are two consequences to this problem. First, as  $d/r_0$  becomes greater than about 1, tilts across the subapertures are more likely to exceed 2π and SRI WFS performance will degrade because it cannot measure the wavefront accurately. This is why a Shack-Hartmann WFS performs better than a SRI WFS in simulations where scintillation is weak and  $d/r_0 \gtrsim 1$ .<sup>6,7</sup> Second, if a continuous surface DM is being controlled with one SRI WFS subaperture per actuator and commands between neighboring actuators exceed a 2π phase difference (e.g., when attempting to approximate branch cuts on the DM) the SRI WFS will not sense the phase differences very well. In some simulations, these large phase differences continued to build up on the DM and, without any positive feedback to properly control them, continued to grow unchecked until stopped by the physical limits of the simulated DM hardware. Events similar to these also have been observed during laboratory experiments.

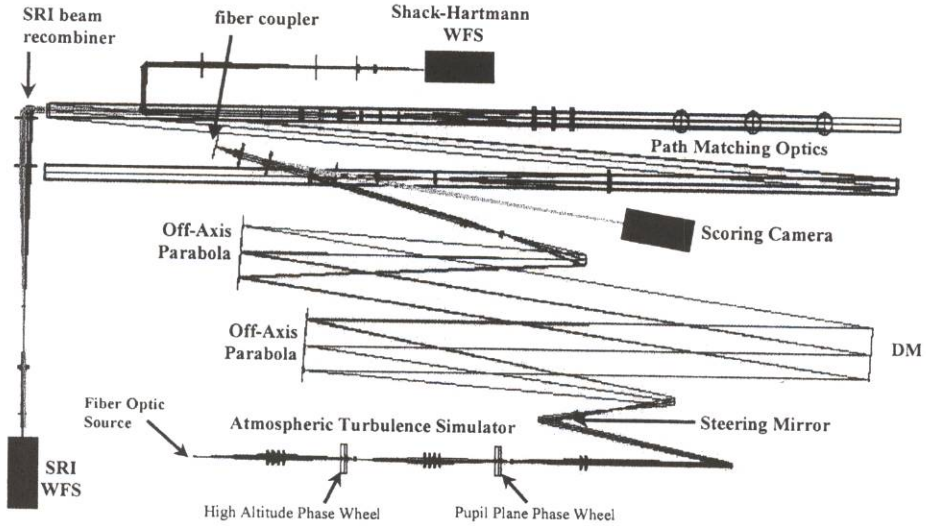


Figure 4. Optical design for the SRI WFS laboratory demonstration.

One way to reduce the likelihood of problems occurring due to large tilts is to over sample the wavefront, creating a high-resolution SRI WFS with a  $2 \times 2$  (or larger) block of subapertures for each DM actuator as shown in figure 2(b). The increased resolution reduces the  $d/r_0$  ratio and moves wavefront sensing performance higher up on the performance curve shown in figure 3. When problems associated with large tilts have occurred in simulations or in the lab, changing to the high-resolution SRI WFS configuration has alleviated the problem. Unfortunately, it is not always possible or simple to increase the WFS resolution. Therefore, it may be beneficial to develop smarter reconstructors which consider the DM commands along with the WFS data.

#### 4. LABORATORY DEMONSTRATION

The overall objective of the SRI WFS project is to develop an understanding of the practical issues involved in fabricating and operating a SRI WFS. The first phase of the project applied a combination of theoretical analysis and numerical simulation to establish an understanding of SRI WFS characteristics and performance. With that phase complete, we have moved on to the second phase and begun constructing a laboratory test facility for demonstrating the SRI WFS and evaluating its performance in hardware. The goal is to use the demonstration to strengthen our understanding of the SRI WFS and to validate and anchor the analyses and simulations using laboratory results.

To fully evaluate the SRI WFS over as many of the configuration and component options mentioned above as possible, we had to construct a platform where it could be evaluated in a realistic and reproducible environment. With this objective in mind, over the last year we have been constructing the Atmospheric Simulation and Adaptive-optics Laboratory Testbed (ASALT). The goal of the design process, both in terms of optics and electronics, was flexibility. The ASALT was designed to allow testing over a wide range of operational scenarios in order to evaluate SRI WFS performance and determine the most favorable design and configuration parameters. The optical design for the SRI WFS testbed is shown in figure 4. The main components of the testbed are described below. Testing of the SRI WFS is in progress and some preliminary results are presented in section 5.

##### 4.1. Atmospheric turbulence simulator

To perform tests in the presence of turbulence, an atmospheric turbulence simulator (ATS) was designed and built for the ASALT. Pictures of the ATS design and hardware are shown in figure 5. The ATS simulates a two-layer atmosphere using static phase plates imprinted with Kolmogorov statistics and is capable of generating a wide range of atmospheric conditions.<sup>11</sup> The phase plates are located in the middle of two, back-to-back afocal systems. By placing the phase plates in converging portions of the beam, the magnitude of  $r_0$  can be controlled by moving the plates up or down the beam path. In addition, scintillation can be controlled by selecting appropriate

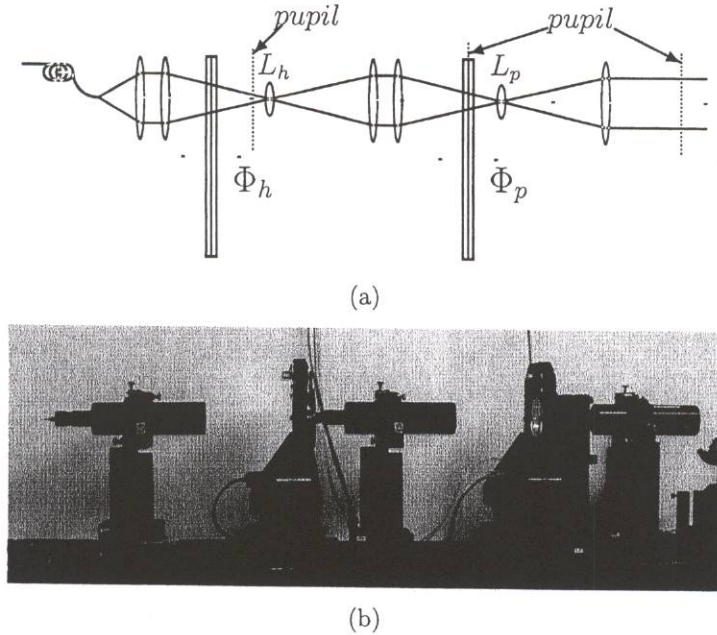


**Figure 5.** (a) Conceptual design for the atmospheric turbulence simulator and (b) a picture of the hardware. The fiber input is shown on the left. The static phase plates ( $\Phi_h$  and  $\Phi_p$ ) are held in mounts between three lens tubes which, in turn, hold the relay lenses and field lenses ( $L_h$  and  $L_p$ ).

field lenses for each afocal system to adjust the effective altitude of the turbulence. To adjust the Greenwood frequency, the phase plates are rotated through the optical beam by computer-controlled stepper motors. The motors control the rotation position and speed of the plates, allowing turbulence scenarios to be repeated. A more detailed discussion of the ATS design and operation can be found in a separate conference paper.<sup>12</sup>

#### 4.2. Deformable mirror

After exiting the ATS, the aberrated beam is relayed onto a steering mirror and then onto the DM. Both mirrors are conjugate to the system pupil. Off-axis parabolas are used to relay and resize the beam before and after reflection from the DM. The DM is a Xinetics 577-channel continuous surface mirror with  $4\mu\text{m}$  of physical stroke and a 7 mm actuator spacing. The pupil diameter at the DM is 140 mm allowing 21 actuators to fit across the beam. The DM is capable of operating at several kilohertz but, because commercial IR cameras from Indigo are used for the WFS and focal plane scoring cameras, the system frame rate is limited to a few tens of Hertz.

#### 4.3. SRI WFS

The testbed is designed to accommodate at least two WFSs—an SRI WFS and a Shack-Hartmann WFS. Currently only the SRI WFS is integrated and aligned in the system. The Shack-Hartmann sensor will be added in the next few months to allow comparison testing between the two.

At present, the SRI WFS is configured as depicted in figure 1. After correction by the steering mirror and DM, part of the optical beam is coupled into a single mode fiber to form the reference and part is used for the beacon. A small part ( $\approx 10\%$ ) of the power coupled into the fiber is sent to a photodiode to determine coupling efficiency and the on-axis Strehl ratio of the corrected beam. The rest of the coupled power is used for the reference. The components in the reference fiber path include an optical isolator, an optical amplifier, a fiber phase shifter, and a narrow-band (0.3 nm) spectral filter. These components are shown in figure 6. The isolator is needed to ensure ASE from the amplifier does not back propagate through the system and cause problems with the input laser source or any detectors in the setup. At the output of the fiber path, a lens is used to collimate the reference so it can be recombined with the beacon beam on the SRI WFS camera.

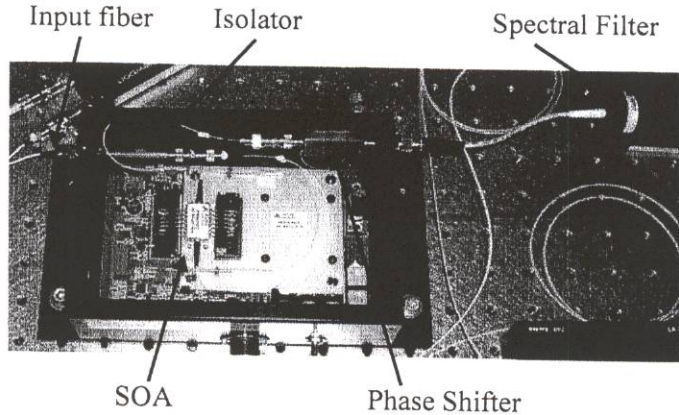


Figure 6. Components of the SRI WFS fiber path.

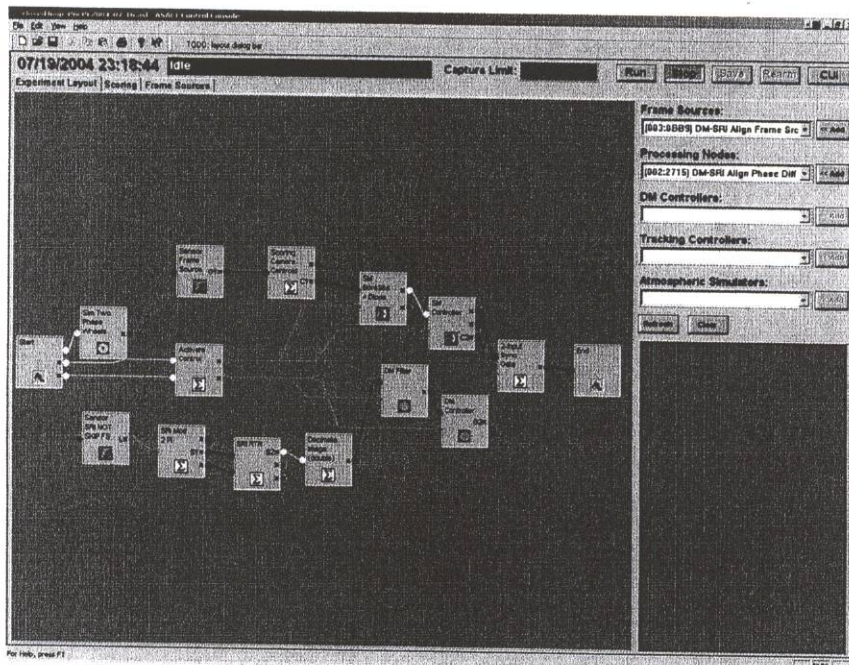
For optical amplifiers, we have a SOA and an EDFA available for testing. The SOA is a commercial device (from InPhenix) with a maximum gain of about 20 dB, a noise figure of 9 dB, and a fiber length of about 50 cm including the fiber pigtailed. The EDFA is a custom unit (from MPB) with 20 dB gain, a noise figure near 3 dB, and a fiber length of 10 m. The EDFA was customized by cutting a 20 m EDFA with 40 dB gain in half and adjusting components so as to retain the original 3 dB noise figure. This customization was done because our analysis showed a gain of 40 dB was not needed and the path matching requirements for a 20 m fiber length were prohibitive. At present, use of the 10 m EDFA requires bouncing the beacon beam up and down the optical table several times. As indicated in figure 4, the lenses, mirrors, and mounts required to do this make up a large portion of the overall design.

The SRI WFS currently implements temporal phase shifting. With only minor adjustments to the optical system, the combined temporal and spatial phase shifting approach mentioned in section 3 can be implemented in the hardware. However, since data flow and processing are controlled and synchronized by the computer system as described below, any of the three phase shifting approaches discussed in section 3 can be simulated using the current setup. For the experimental results presented below, spatial phase shifting was simulated by capturing all four of the interference images during the same time step of the AO system control loop. The camera used for the SRI WFS is a large-format Phoenix camera from Indigo and the detector readout is windowed down to a 200x200 array so that it is capable of running at about 200 Hz. When simulating spatial phase shifting, the data frame rate can be as high as 50 Hz, although computations for wavefront reconstruction and tracking slow the rate to about 20 Hz.

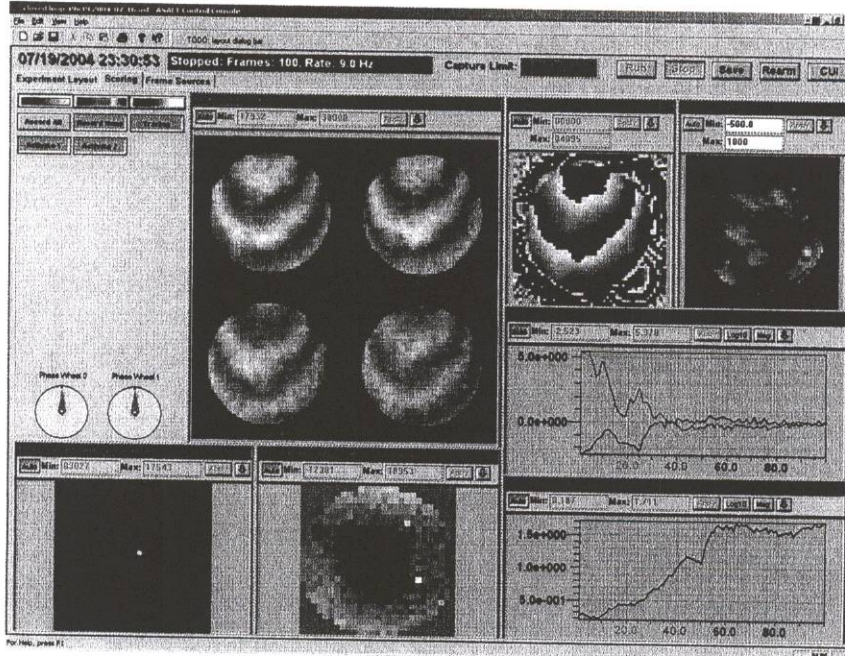
#### 4.4. Control system

The ASALT control system was designed to provide a well-defined, flexible architecture for integrating and linking hardware and software elements. To realize this goal, a modular architecture was developed. The basic building block of the system is a component, which is similar to an object in object-oriented programming. Components can be things such as frames sources (i.e., sensors and detectors), DM controllers, tracking controllers, atmospheric simulators, and processing nodes. Each component has defined input and output data interfaces to which other components connect as demonstrated in figure 7(a). This figure shows the control console layout screen with a setup for a SRI WFS closed-loop experiment. Components are dropped into the layout window and linked together to perform a desired function. The boxes represent active components and the lines between them indicate the flow of data. The underlying application programming interface (API) controls the flow and synchronization of data between components, ensuring that only compatible inputs and outputs are connected and that a component is initiated only when all of its inputs are satisfied.

In developing the system, flexibility and simplicity of use were given higher priority than speed. All of the components for the SRI WFS testbed are run on personal computers, although it is possible to incorporate other platforms. Reflective memory is used to pass information between the computers. Whenever one computer in the network writes to its reflective memory card, the data gets replicated on all the other computers in the



(a)



(b)

**Figure 7.** Screen captures from the ASALT control console. (a) Experiment layout screen. A SRI WFS closed-loop layout is shown. The lower path represents the higher-order DM correction and the upper path represents tracking. (b) Data display screen for SRI WFS closed-loop layout in (a). Data from a SRI WFS, wavefront reconstruction, DM, tracking, scoring camera, and power in the fiber are shown. This example is for the  $41 \times 41$  SRI WFS configuration.

**Table 1.** Atmospheric scenarios used for initial SRI WFS tests.

Atmosphere	$r_0$ (cm) <sup>†</sup>	$\sigma_X^2$	$f_G$ (Hz) <sup>‡</sup>	$d_{WFS}/r_0$		$d_{DM}/r_0$	$f_G/f_{3dB}$
				21 × 21	41 × 41		
A	26.3	0.003	30	0.24	0.12	0.24	0.66
B	19.1	0.121	30	0.33	0.16	0.33	0.66
C	17.0	0.186	30	0.37	0.19	0.37	0.66
D	15.0	0.272	30	0.42	0.21	0.42	0.66
E	11.9	0.492	30	0.53	0.26	0.53	0.66
F	9.8	0.757	30	0.63	0.32	0.63	0.66
G	7.6	1.290	30	0.82	0.41	0.82	0.66

<sup>†</sup> Value of  $r_0$  based on 1.25 m aperture diameter. <sup>‡</sup> Value of  $f_G$  based on 1 kHz AO system.

network at 2.12 Gbaud. Writing and reading data from the reflective memory is handled by the API through a set of library functions created for use within each component's software interface. Any component can run on any computer in the network and multiple components can run on the same computer. However, if a component controls a piece of hardware, it must run on a computer capable of controlling that hardware. If more processing power is needed, more computers can be added to the network.

A graphical interface has been integrated into the control console. Any data written to the reflective memory can be displayed as shown in figure 7(b). This figure shows the graphical display corresponding to the layout shown in (a). For the data run shown, tracking was turned on at frame 25 and the higher-order AO at 50. The plots in the lower right show the effect these events had on the power in the fiber (bottom strip chart) and the tracker centroid position (top strip chart). The other displays correspond to the state of the system—WFS output, wavefront reconstruction, scoring image, and DM commands—at frame 100. The display is useful for validating component functionality and system operation. The data can also be saved for later analysis. During operation, the API keeps a history of each component's outputs on the local computer. At the conclusion of a run, this data can be transferred to the main control computer for storage in a common capture file.

## 5. PRELIMINARY TEST RESULTS

Construction of the ASALT system has proceeded at a good pace. We initially closed the AO loop with the SRI WFS at the end of February 2004 and since then have been working up the system alignment and functionality. Actual testing of the SRI WFS is in progress but has only recently begun in earnest. This section presents some preliminary results from those tests. A more thorough and wide ranging evaluation of SRI WFS performance will be carried out in the next few months.

For the data presented below, the ATS was used to create a series of atmospheric scenarios as shown in table 1. The table gives values for the atmospheric coherence length ( $r_0$ ), Rytov number ( $\sigma_X^2$ ), and Greenwood frequency ( $f_G$ ). These parameters were obtained from a numerical model of the ATS (which we are in the process of calibrating against laboratory measurements).<sup>12</sup> All three atmospheric parameters are theoretical values calculated from the  $C_n^2$  profile. The values of  $r_0$  and  $f_G$  are scaled to correspond to a telescope aperture of 1.25 m and a frame rate of 1 kHz. The Rytov numbers do not include saturation effects which limit the observed log-amplitude variance to a maximum value of about 0.3.

The AO system was configured with 21 DM actuators across the pupil. The pixel scale on the scoring camera was about  $\lambda/4D$ , where  $D$  is the aperture size. The SRI WFS was tested in both low and high-resolution modes with 21 and 41 subapertures across the pupil. The AO control system only used the least-squares portion of the reconstructed phase ( $\tilde{\phi}_b^{LS}$  from equation 24) to control the DM. The SRI WFS was run in a simulated spatial phase-shifting mode as described above, and each reconstruction of the WFS data was used to update the DM commands for the next frame of data. We were mainly interested in looking at performance with respect to  $r_0$  and scintillation, so we did not attempt to optimize the control-loop bandwidth  $f_{3dB}$ . Table 1 also shows the performance parameters related to this setup.<sup>13</sup> The ratio of the WFS subaperture size  $d_{WFS}$  to  $r_0$  gives an indication of wavefront sensing accuracy as shown in figure 3. The ratio of the DM actuator spacing  $d_{DM}$  to  $r_0$  gives an indication of DM fitting error. The ratio of  $f_G$  to the system bandwidth  $f_{3dB}$  gives an indication of the

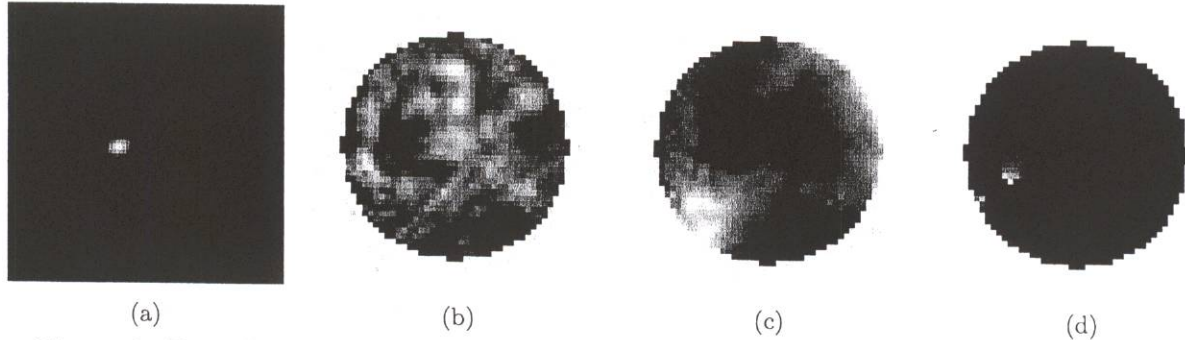


**Figure 8.** Example wavefront sensing data from the SRI WFS. The figures show (a) the PSF, (b) the amplitude, (c) the least-squares phase, and (d) the branch point phase for the measured wavefront. These data were captured using Atmosphere E and the  $41 \times 41$  SRI WFS. Tracking was enabled but higher-order AO was not. In figure (d), the white and black colors correspond to  $\pi$  and  $-\pi$  phase levels, respectively.

performance loss due to latency and temporal evolution of the turbulence. In addition, the illumination level at the SRI WFS camera was made high enough so that camera noise was not expected to be an issue except as a result of scintillation. Amplification of the reference beam was done using the SOA with the pump current set to produce a gain of about 16 dB.

A snapshot of captured SRI WFS data is shown in figure 8. The figure shows a point spread function (PSF) from the scoring camera along with the corresponding WFS amplitude and phase reconstructions. These data were collected with the  $41 \times 41$  SRI WFS under moderate scintillation. The peak-to-valley of the least-square phase is  $1.2\lambda$  with an rms of  $0.37\lambda$ . The branch-point phase shows two branch point pairs on the left side of the aperture connected by branch cuts. For these data the track loop was enabled but the higher-order AO loop was not. However, the AO system was enabled at this frame (frame 50) and was able to successfully close the loop within a few frames, as seen in figure 9. This result indicates that, with a moderate level of scintillation and with branch points present, the wavefront reconstruction was of sufficient quality that compensation of the wavefront phase aberrations could occur and the AO loop could be closed successfully.

Figure 9 shows data from a closed-loop scenario using the SRI WFS. Average PSF images are shown for open-loop and closed-loop operation with both the low-resolution ( $21 \times 21$ ) and high-resolution ( $41 \times 41$ ) SRI WFS configurations. The data sequences were added, without shifting, to create these images. The closed-loop images are near diffraction limited. A time history is also shown of the measured power in the fiber, as represented by the amplifier output voltage from the photodiode mentioned above. The times at which the track and AO loops were enabled are indicated. The graph shows how the fiber coupling performance improved as the track loop was closed and again when the AO loop was closed. The graph also shows that the high-resolution SRI WFS performed noticeably better than the low-resolution SRI WFS in this particular case, and that both of them were much better compared to the open-loop performance.

Performance of the AO system for the atmospheric scenarios listed in table 1 is shown in figure 10. For these tests, each data collection was 200 frames long. Like the example shown in figure 9, tracking was enabled at frame 25 and higher-order AO at frame 50. Performance was determined by averaging the scoring camera images for the last 100 frames. The system operated at about 20 Hz so the peak of each image was shifted to a common point before averaging in order to compensate for the small amount of jitter caused by lab turbulence. To produce the Strehl ratios shown in the figure, a “perfect” reference image was created by injecting a uniform, collimated beam of the appropriate diameter into the optical train of the scoring camera. The Strehl ratios were calculated by comparing the average images with this reference image.

Part (a) of figure 10 shows that as the turbulence strength increased (i.e., from scenario A to G  $r_0$  decreased and  $\sigma_x^2$  increased) the level of AO compensation decreased. As expected from the discussion in section 2, the high-resolution SRI WFS outperformed the low-resolution SRI WFS because it better samples the wavefront. Part (b) of the figure plots Strehl as a function of  $d_{WFS}/r_0$ . From figure 3, one might expect the two curves to lay on top of each other with the curve for the  $41 \times 41$  SRI WFS falling on the upper right end of the curve

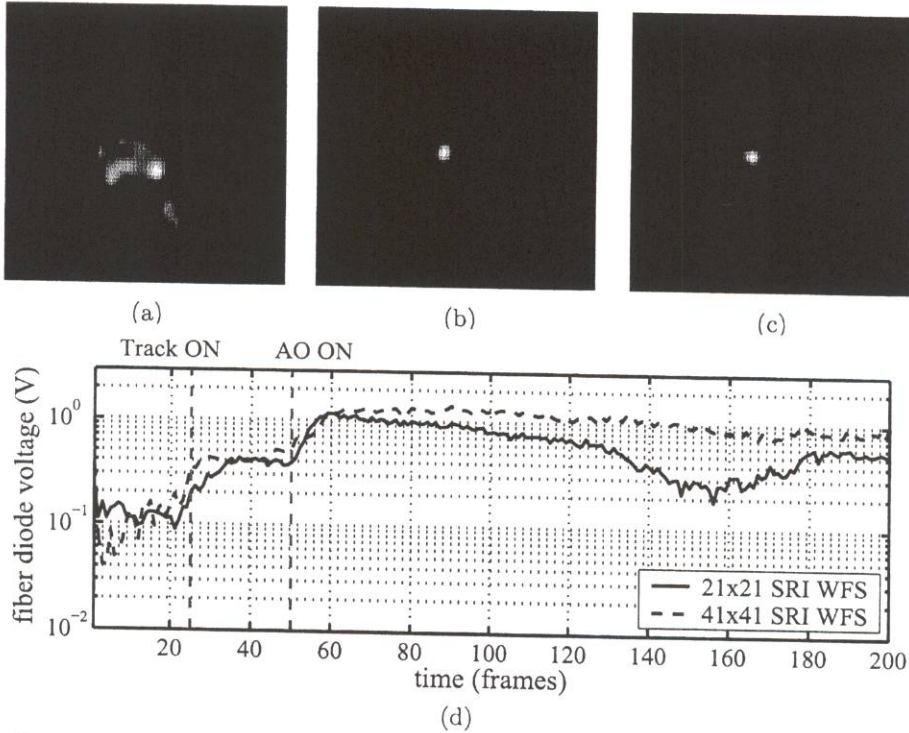


**Figure 9.** Example closed-loop results for the SRI WFS. The top three figures show the average PSF for (a) open loop, (b) closed loop with a  $21 \times 21$  SRI WFS, and (c) closed loop with a  $41 \times 41$  SRI WFS. The images are averaged over the last 100 frames of each data collection. The bottom plot shows the output of the photodiode measuring the power coupled into the SRI reference fiber for the two closed loop scenarios.

for the  $21 \times 21$  case. This is not the case because figure 3 is related to wavefront sensing performance only and not overall AO performance. The DM is able to correct phase aberrations, but not scintillation. Overall AO performance is expected to depend on the strength of scintillation according to  $\exp(-\sigma_x^2)$ , where  $\sigma_x^2$  is the observed log-amplitude variance. A correction for this dependence can be applied to the data by taking the Rytov numbers from table 1, saturating them at 0.3, and dividing the Strehl ratios by  $\exp(-\sigma_x^2)$ . The result of this calculation is shown in part (c) of the figure. This graph shows that the Strehl ratios for the two WFS configurations do indeed follow the same curve after scintillation effects are taken into consideration.

The data presented above show encouraging results for the performance of the SRI WFS. However, they are limited in scope. Over the next few months tests will be run over a wider range of atmospheric scenarios and operating conditions of the AO system. Among other things, these tests will examine different WFS resolutions, phase shifting methods, wavefront reconstruction algorithms, and the effect of signal-to-noise on performance. Also, once the Shack-Hartmann WFS is integrated, comparison testing between the two WFSs will commence.

## 6. CLOSING COMMENTS

This paper discussed the design and operation of a SRI WFS. Practical issues related to the design, fabrication, and performance of the SRI WFS were discussed. Previous analysis and simulation efforts have shown that the SRI WFS is capable of providing superior performance compared to conventional WFSs in strong scintillation environments. During the last year, we have been developing and constructing a laboratory facility in order to evaluate the SRI WFS and validate these previous analyses. The ASALT provides a well-controlled and flexible laboratory environment for the design, development, and testing of advanced AO concepts and technologies like the SRI WFS.

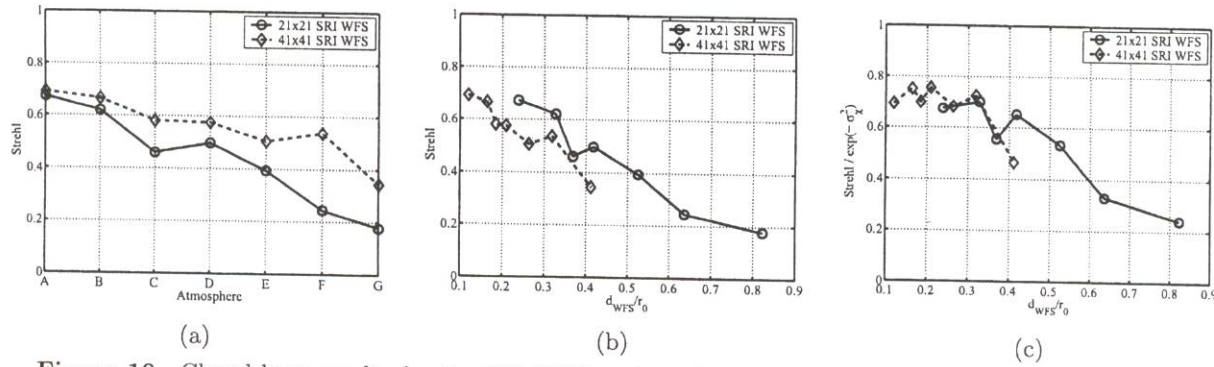


**Figure 10.** Closed-loop results for the SRI WFS evaluated over different atmospheric conditions. The figures show the (a) amplitude, (b) least-squares phase, and (c) branch point phase of the wavefront. These data are for Atmosphere E with the  $41 \times 41$  SRI WFS. Tracking was on but higher-order AO was off.

Evaluation of the SRI WFS is in progress and some preliminary results were presented. Further testing is necessary and will be carried out over the next several months. These tests will include SRI WFS evaluation and performance comparison with the Shack-Hartmann sensor over a wider range of atmospheric scenarios, operating conditions, phase shifting configurations, and AO control loop parameters. We also plan to look at the ability to correct for branch points in the wavefront phase. Lastly, we continue to add functionality to the system so that more efficient calibration and testing can be performed. In the future, we hope to use the ASALT to test and develop other AO concepts and technologies.

## REFERENCES

1. J. W. Hardy, *Adaptive Optics for Astronomical Telescopes*, Oxford U. Press, Oxford, 1998.
2. D. L. Fried, "Branch point problem in adaptive optics," *J. Opt. Soc. Am. A* **15**, pp. 2759–2768, 1998.
3. J. D. Barchers, D. L. Fried, and D. J. Link, "Evaluation of the performance of Hartmann sensors in strong scintillation," *Appl. Opt.* **41**, pp. 1012–1021, 2002.
4. J. D. Barchers, D. L. Fried, and D. J. Link, "Evaluation of the performance of a shearing interferometer in strong scintillation in the absence of additive measurement noise," *Appl. Opt.* **41**, pp. 3674–3684, 2002.
5. J. D. Barchers, D. L. Fried, D. J. Link, G. A. Tyler, W. Moretti, T. J. Brennan, and R. Q. Fugate, "Performance of wavefront sensors in strong scintillation," *Proc. SPIE* **4839**, pp. 217–227, 2003.
6. T. A. Rhoadarmer and J. D. Barchers, "Noise analysis for complex field estimation using a self-referencing interferometer wave front sensor," *Proc. SPIE* **4825**, pp. 215–227, 2002.
7. J. D. Barchers and T. A. Rhoadarmer, "Evaluation of phase-shifting approaches for a point diffraction interferometer using the mutual coherence function," *Appl. Opt.* **41**, pp. 7499–7509, 2002.
8. D. Malacara, *Optical Shop Testing*, Wiley, New York, 1992.
9. A. N. Kolmogorov, "The local structure of turbulence in incompressible viscous fluids for very large Reynolds' numbers," in *Turbulence, Classic Papers on Statistical Theory*, S. K. Friedlander and L. Topper, eds., pp. 151–155, Wiley-Interscience, New York, 1961.
10. R. H. Hudgin, "Wave-front reconstruction for compensated imaging," *J. Opt. Soc. Am.* **67**, pp. 375–378, 1977.
11. S. M. Ebstein, "Pseudo-random phase plates," *Proc. SPIE* **4493**, pp. 150–155, 2002.
12. S. J. Mantravadi, T. A. Rhoadarmer, and R. S. Glas, "A simple laboratory system for generating well-controlled atmospheric-like turbulence," *Proc. SPIE* **5553**, in press.
13. R. Q. Fugate, "Atmospheric compensation," *International Trends in Applied Optics*, A. H. Guenther, ed., pp. 539–569, SPIE, (Bellingham), 2002.